Modeling Intrajunction Dispersion at a Well-Mixed Tidal River Junction

Phillip J. Wolfram[1]; Oliver B. Fringer[2]; Nancy E. Monsen[3]; Karla T. Gleichauf[4]; Derek A. Fong, A.M.ASCE[5]; and Stephen G. Monismith, A.M.ASCE[6]

Abstract: The relative importance of small-scale, intrajunction flow features such as shear layers, separation zones, and secondary flows on dispersion in a well-mixed tidal river junction is explored. A fully nonlinear, nonhydrostatic, and unstructured three-dimensional (3D) model is used to resolve supertidal dispersion via scalar transport at a well-mixed tidal river junction. Mass transport simulated in the junction is compared against predictions using a simple node-channel model to quantify the effects of small-scale, 3D intrajunction flow features on mixing and dispersion. The effects of three-dimensionality are demonstrated by quantifying the difference between two-dimensional (2D) and 3D model results. An intermediate 3D model that does not resolve the secondary circulation or the recirculating flow at the junction is also compared to the 3D model to quantify the relative sensitivity of mixing on intrajunction flow features. Resolution of complex flow features simulated by the full 3D model is not always necessary because mixing is primarily governed by bulk flow splitting due to the confluence–diffluence cycle. Results in 3D are comparable to the 2D case for many flow pathways simulated, suggesting that 2D modeling may be reasonable for nonstratified and predominantly hydrostatic flows through relatively straight junctions, but not necessarily for the full junction network. **DOI: 10.1061/(ASCE)HY.1943-7900.0001108.**

Introduction: Dispersion in Channel Junctions

A junction joins distinct channels so that flows are either combined, as in the case of a confluence, or separated, as in the case of a diffluence. This confluence–diffluence cycle is dependent upon tidally oscillating flow conditions that drive bulk flows through the system and redirect flow from one channel to another (Weber et al. 2001; Ramamurthy et al. 2007; Neary and Sotiropoulos 1996). Flow phasing leads to opposite-directed flows in different junction branches and ultimately determines the spatio-temporal distribution of intrajunction features such as shear layers and separation zones (Gleichauf et al. 2014).

Intrajunction flow features commonly arise due to flow curvature induced by junction geometry and the relative flow rates of channels in the composite confluence–diffluence. Flow separates and forms recirculation zones at junction walls for sufficiently high flow rates and strong curvature. Horizontal shear-driven mixing layers arise in the interior of the junction due to differences in inflow and outflow channel flow rates. The resultant shear plane may tilt transverse to the flow due to local imbalances between centrifugal acceleration and transverse bottom friction (Weber et al. 2001). Variation in channel bathymetry, or discordances, allows formation of a vertical shear layer which can be effective in enhancing mixing (Bradbrook et al. 2001). Provided the flow is strong enough and the bathymetry is steep enough, separation and upwelling may occur in the vertical (Best and Roy 1991).

Although several studies have analyzed dispersion in highly idealized junctions (Smith and Daish 1991; Bradbrook et al. 2001; Biron et al. 2004), the relative contributions of complex intrajunction flow features to dispersion are largely unknown, particularly for a real-world, field-scale junction. Improved understanding of dispersion in junctions is needed because management decisions related to ecosystem health commonly rely upon simplified models, e.g., assuming complete mixing at junctions in simple node-channel hydrodynamics models like the Delta Simulation Model 2 (CA DWR 1998; Kimmerer and Nobriga 2008). Progress on improved intrajunction mixing models has been limited due to spatio-temporal flow complexity, making measurement and modeling difficult because of sharp gradients and intermittency in space and time.

To the authors' knowledge, this is the first detailed numerical study of intrajunction flow feature contributions to junction mixing. The main purpose of the study is to examine the conditions needed

[1]Research Assistant, Bob and Norma Street Environmental Fluid Mechanics Laboratory (EFML), Dept. of Civil and Environmental Engineering, Stanford Univ., 473 Via Ortega, Stanford, CA 94305; Postdoctoral Research Associate, Climate, Ocean and Sea Ice Modeling (T-3), Los Alamos National Laboratory, Los Alamos, NM 87544 (corresponding author). E-mail: pwolfram@lanl.gov

[2]Associate Professor, Bob and Norma Street Environmental Fluid Mechanics Laboratory (EFML), Dept. of Civil and Environmental Engineering, Stanford Univ., 473 Via Ortega, Stanford, CA 94305. E-mail: fringer@stanford.edu

[3]Research Associate, Bob and Norma Street Environmental Fluid Mechanics Laboratory, Dept. of Civil and Environmental Engineering, Stanford Univ., 473 Via Ortega, Stanford, CA 94305. E-mail: nemonsen@stanford.edu

[4]Research Assistant, Bob and Norma Street Environmental Fluid Mechanics Laboratory (EFML), Dept. of Civil and Environmental Engineering, Stanford Univ., 473 Via Ortega, Stanford, CA 94305. E-mail: kgleich@stanford.edu

[5]Senior Research Engineer and Lecturer, Bob and Norma Street Environmental Fluid Mechanics Laboratory (EFML), Dept. of Civil and Environmental Engineering, Stanford Univ., 473 Via Ortega, Stanford, CA 94305. E-mail: dfong@stanford.edu

[6]Professor, Bob and Norma Street Environmental Fluid Mechanics Laboratory (EFML), Dept. of Civil and Environmental Engineering, Stanford Univ., 473 Via Ortega, Stanford, CA 94305. E-mail: monismith@stanford.edu

Note. This manuscript was submitted on November 3, 2014; approved on September 16, 2015; published online on April 6, 2016. Discussion period open until September 6, 2016; separate discussions must be submitted for individual papers. This paper is part of the ***Journal of Hydraulic Engineering***, © ASCE, ISSN 0733-9429.

to compute intrajunction transport over supertidal timescales, i.e., a single flow-through in the junction with length scales much less than the tidal excursion and time scales much less than the full semidiurnal tide (<6 h). This approach tests the impact of simulating transport in the junction affected by small-scale features with high time and space resolution. Consequently, multiple scalar samplings of the junction over the full tidal cycle and length scales on the order of the tidal excursion are not evaluated. Such processes are highlighted by Gleichauf et al. (2014), who discuss how flow phasing is an important driver of mixing at subtidal time scales. The role of high-resolution, three-dimensional modeling relative to common modeling simplification and assumptions is assessed by quantifying variances in time-varying scalar fate in the junction. Grid resolution requirements, the validity of two-dimensional versus three-dimensional modeling, the role of intrajunction flow features, and the applicability of a node-channel model approximation are assessed by comparing the results to high-resolution modeling of junction dispersion to evaluate suitability of these assumptions to characterize mixing.

In this paper, an exploration of junction dispersion begins with a description of junction hydrodynamics and secondary flow features at the Georgiana Slough Junction field site. Computational methods and model validation via field observations (Gleichauf et al. 2014) are then presented, followed by an examination of the applicability and implications of many commonly used modeling assumptions. Concluding remarks summarize the relative importance of small-scale intrajunction flow features and simplified modeling assumptions on dispersion.

Background: Georgiana Slough Junction

The Georgiana Slough Junction (GSJ) in the Sacramento-San Joaquin Delta, California serves as a case study to understand junction dispersion in a nonstratified flow. The channel geometry of the Delta, shown in Fig. 1(a), is complex, and the resultant tidal river flows are dependent on riverine, tidal, and water import and export forcing (MacWilliams et al. 2015). The flow in GSJ is dependent on Delta Cross Channel (DCC) gate operations [Fig. 1(b)] and is formed by joined and separated flows of the Georgiana Slough River (GES), the North Mokelumne River (NMR), the South Mokelumne River (SMR), and the Mokelumne River (MOK) [Fig. 1(c)]. GSJ is predominantly shallow (2–3 m) with a mean depth of 5 m; however, it has dynamic bathymetry that ranges from 2 m within the junction to 10 m in upstream tributaries, including a maximum depth of 20 m in a scourhole at the confluence of GES and MOK [Fig. 1(c)].

Field observations, collected via acoustic Doppler current profilers (ADCPs) were taken at locations also specified in Fig. 1(c). These observations, combined with a modeling study that is the precursor to the present work, demonstrate that the GSJ exhibits both confluence and diffluence behavior with flow features identified in the field study by Gleichauf et al. (2014). Figs. 1(d and e) schematically illustrate the flow features occurring during ebb and flood tide, respectively. These features occur on supertidal time scales (timescales occurring faster than tidal timescales) due to flow amplitude and phase variability and are discussed following the validation of the numerical model.

The strength of these intrajunction flow features is dependent upon DCC gate operations. The GSJ is the primary junction downstream of the DCC, a diversion channel that transfers flow rates up to 100 $m^3 s^{-1}$ (approximately 10% of the Sacramento River's discharge) from the Sacramento River into the Mokelumne River feeding GSJ [Fig. 1(a)]. DCC gate operations affect mixing by modifying the flows forcing GSJ, as shown in Fig. 1(b). For example, river-flow forcing is enhanced in the NMR and SMR when the DCC is open relative to when the DCC is closed. Consequently, separate periods when the DCC is open and closed during the June 2012 field campaign are used for analysis in this modeling study.

Methods: Simulating Intrajunction Dispersion in the Georgiana Slough Junction

Numerical Modeling and Parameterizations

Intrajunction flow features within GSJ are simulated with the parallel, Stanford Unstructured Nonhydrostatic Terrain-Following Adaptive Navier-Stokes Simulator (SUNTANS) model (Fringer 2006; Fringer et al. 2006) which is capable of simulating depth-averaged and three-dimensional (3D) coastal ocean flows, as given by the Reynolds-Averaged Navier-Stokes (RANS) equations employing the Boussinesq approximation and an eddy-viscosity model. The free-surface continuity and nonhydrostatic momentum equations are discretized on an extruded horizontally unstructured C-grid (i.e., prismatic cells, since SUNTANS employs z-levels in the vertical) to allow simulation of multiscale fluid physics on a shoreline-conforming regional-scale orthogonal triangular C-grid and a junction-scale orthogonal quadrilateral C-grid, with both computational domains shown in Fig. 1(b). Semi-implicit treatment of the free-surface and vertical diffusion via the θ-method (Casulli and Walters 2000; Casulli and Zanolli 2002) eliminates time-step restrictions associated with fast free-surface gravity waves and strong vertical turbulent diffusion in thin vertical layers.

Horizontal viscosity and diffusivity parameterize unresolved sub-grid-scale turbulent diffusion and ensure stability for numerical integration of the central-differenced momentum advection scheme. Previous studies estimated horizontal viscosity for South San Francisco Bay, Boston Harbor, and the Snohomish River estuary, with values ranging from 0.1 to 1.0 $m^2 s^{-1}$ (Signell and Butman 1992; Gross et al. 1999; Wang et al. 2009). Consistent with these criteria, different diffusivities are used for a regional-scale domain bounded by gauging stations and a nested junction-scale domain resolving intrajunction flow features (detailed in the next section). A horizontal diffusivity of 3.5×10^{-1} $m^2 s^{-1}$ is used for the regional-scale domain. A diffusivity of 5.0×10^{-2} $m^2 s^{-1}$ is used for the junction-scale domain to resolve the higher effective Reynolds number characteristic of intrajunction flow features. Vertical viscosity and diffusivity are obtained via the Mellor and Yamada (1982) Level 2.5 turbulence closure scheme.

The bottom shear stress boundary condition assumes a vertical velocity profile consistent with the log-law to ensure that computed depth-integrated bottom shear stresses are independent of vertical resolution (Wang et al. 2009). The applied drag coefficient for the 3D simulations is given by

$$C_{d,3D} = \left[\frac{1}{\kappa}\ln\left(\frac{z_b}{z_0}\right)\right]^{-2} \quad (1)$$

where z_b = vertical distance between the bed and cell centroid of the bottommost cell. A constant bed roughness height of $z_0 = 2.5 \times 10^{-4}$ m ($C_{d,3D} = 0.0024$ at 1 m above bed) is employed (Wang et al. 2009, 2011). No drag is applied at vertical cell faces (i.e., at shorelines or channel sidewalls). For two-dimensional simulations, the drag coefficient is determined from the depth-integrated log-law to give

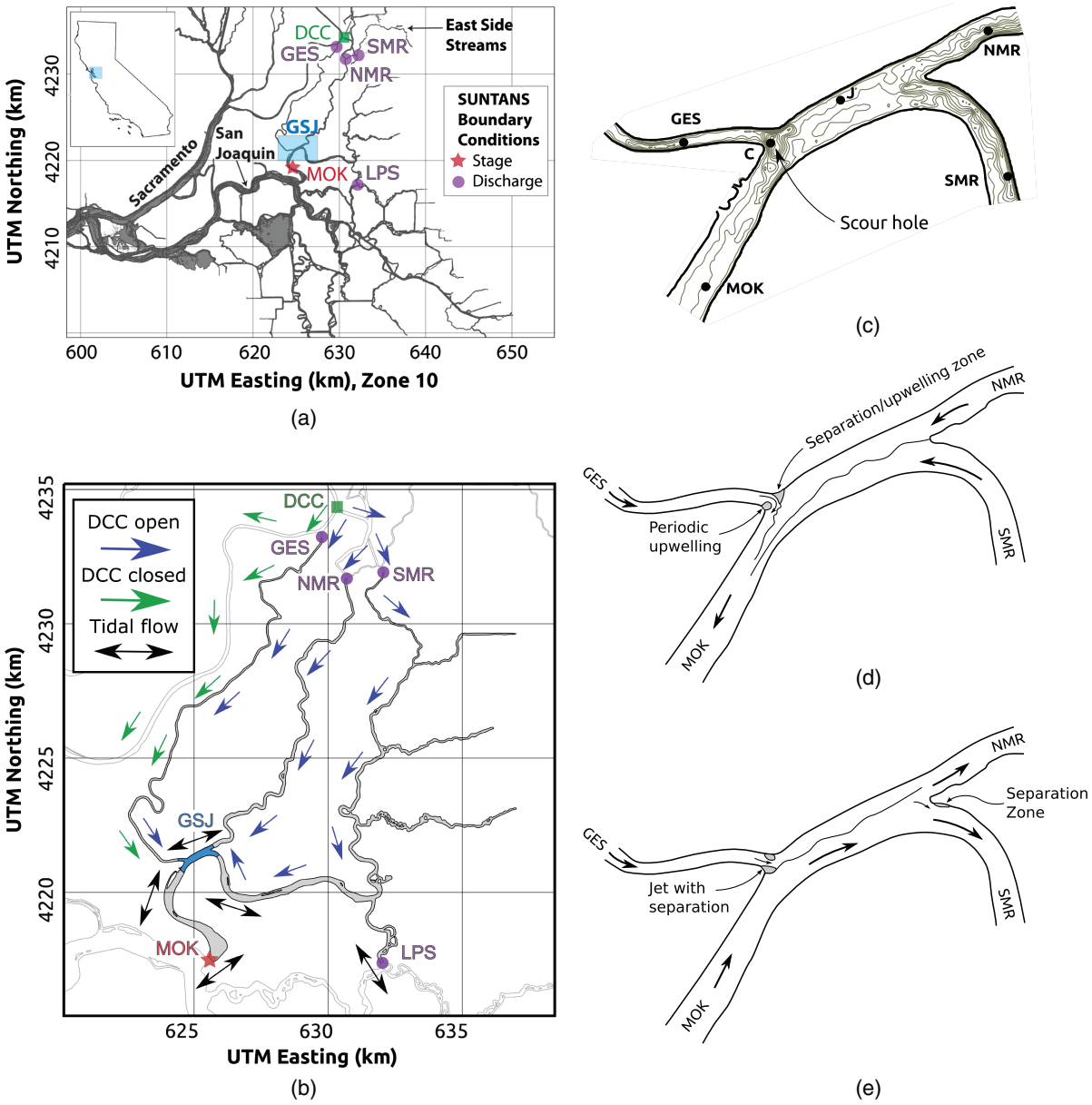

Fig. 1. (Color) Study area: (a) Sacramento-San Joaquin River Delta [adapted from Gleichauf et al. 2014 (http://creativecommons.org/licenses/by/4.0/)]; Georgiana Slough Junction (GSJ) is boxed in blue; map coordinates are in North American Datum 1983 (NAD83), Universal Transverse Mercator (UTM) Zone 10N; (b) regional-scale (in gray) and junction-scale (in blue) GSJ computational domains with arrows designating river flows under typical DCC operations when open (blue arrows) and closed (green arrows); stage boundary conditions shown with red star (MOK) and discharge boundary conditions with purple circles (GES, NMR, SMR, LPS); location of the Delta Cross Channel (DCC) is shown with the green box; (c) junction bathymetry and ADCPs; bathymetry is designated by isobaths at intervals of 2 m; ADCP mooring locations (GES, MOK, NMR, SMR, J, C) are designated by filled circles; (d) ebb tide flow features; (e) flood tide flow features

$$C_{d,2D} = \left\{ \frac{1}{\kappa} \left[\log\left(\frac{H}{z_0}\right) - \left(1 - \frac{z_0}{H}\right) \right] \right\}^{-2} \tag{2}$$

where H = water depth. Scalar transport is computed with the Total Variation Diminishing (TVD) transport scheme with van Leer flux limiter (Chua and Fringer 2011). Scalar diffusivity is not included because the TVD advection scheme's numerical diffusion is on the same order as physical diffusivity at horizontal resolutions used in this analysis (Chua and Fringer 2011). This assumption is reasonable because the flow is advection dominated. A resolution study is used to demonstrate that grid-scale-dependent numerical mixing does not affect conclusions.

Model Configuration

Model domains were generated by extracting a shoreline and bathymetry from a recent digital elevation map (CA DWR 2012). The regional-scale and junction-scale computational domains used in this study are presented in Fig. 1(b). United States Geological Survey (USGS) discharge and stage observations are used to force the regional-scale domain, shown as gray Fig. 1(b). The regional-scale domain is discretized with a triangular C-grid that conforms to the shoreline and allows increased resolution within the junction. Because the dynamics governing the flow and stage on the regional-scale grid are largely two-dimensional, the flow on the regional-scale domain is computed with a two-dimensional

depth-averaged model ignoring momentum advection, drastically reducing run-time by eliminating the time-step restriction associated with explicit-in-time Eulerian momentum advection. Although the regional-scale C-grid employs triangles, which allow accurate calculation of flow and stage, Wolfram and Fringer (2013) showed that triangular C-grids are unable to accurately compute 3D secondary flows with Eulerian central-differencing for momentum advection. Therefore, the junction-scale domain, shown as blue in Fig. 1(b), is discretized with a high-resolution quadrilateral C-grid. This approach computes secondary flows with a grid that naturally resolves streamwise and transverse flows, has improved nondiffusive momentum advection and utilizes nonhydrostatic pressure without filtering (Wolfram and Fringer 2013). The regional-scale grid is used to derive flow and stage boundary conditions for the smaller, higher-resolution quadrilateral junction-scale domain. A larger domain was also employed for the junction-scale grid but the results did not significantly change and hence, the smaller domain was used for computational efficiency.

The regional-scale grid has a mean horizontal resolution of 8.8 m and is run with a time-step size of 200 s and 10,368 time steps over a 24-day simulation period. The regional-scale time step gives a maximum Courant number of $C = 52$ which is much larger than unity owing to the absence of the explicit calculation of momentum advection. The smaller and finer quadrilateral junction-scale grid has a mean horizontal resolution of 3 m and a vertical resolution of 0.8 m. Owing to the inclusion of explicit momentum advection, the time-step size on the fine grid is 0.25 s, which gives a maximum Courant number of $C = 0.42$. Due to the restrictive time step on the high-resolution grid, this domain is run only for 2.25 days, enough to capture tidal-scale hydrodynamics but still requiring 777,600 time steps, 75 times as many as the two-dimensional (2D) regional-scale grid.

Coarser quadrilateral junction-scale grids with mean horizontal resolution of 6 and 12 m, more representative for practical simulations, are also used to quantify the effects of grid resolution. The 6-m grid is also used to study Reynolds number dependence, two-dimesnional versus three-dimensional behavior, and the flow-weighted mixing model for the junction-scale domain. The effects of these modeling assumption scenarios are compared to the base case which is a three-dimensional simulation on the 6-m grid that has low diffusivity and uses momentum advection and nonhydrostatic pressure solvers. The base case is designed to be comparable to a three-dimensional estuarine simulation used in common practice.

Intrajunction Field Observations Used for Validation

In situ Eulerian and Lagrangian intrajunction measurements were obtained to validate the numerical model (Gleichauf et al. 2014). The Eulerian measurement field campaign occurred from May 30 to June 19, 2012, and used six in situ 1,200 kHz Teledyne RD Instruments (TRDI) ADCP instruments (Poway, California) in GSJ [Fig. 1(c)], corresponding to each GSJ channel (GES, MOK, NMR, SMR, and MOK) and interior locations within the junction (C and J). Stage and currents were sampled at a frequency of 1 Hz with 0.25 m resolution in the vertical. Lagrangian measurements were obtained with drifters on June 1 and June 8, 2012, when the DCC was open and closed, respectively (not shown in the present work). Additional details regarding validation of the numerical model with the ADCP and drifter study that are not included in this study are provided in the field campaign study (Gleichauf et al. 2014).

Scalar Transport Methods

Conservative scalar tracers are used to track the fractional composition of water within the junction. The transport equation for a scalar ϕ_i that is advected by velocity $\boldsymbol{u}$ and originates from boundary $i \in 1, \ldots, N_b$, where N_b is the total number of channels connected to the junction, is

$$\frac{\partial \phi_i}{\partial t} + \nabla \cdot (\boldsymbol{u}\phi_i) = 0 \tag{3}$$

with initial condition at time $t = t_0$ given by $\phi_i(\mathbf{x}, t = t_0) = 1/N_b$, corresponding to an even mixture of water from all channels. Inflow boundary conditions at boundaries $\mathbf{x}_{b,j}$, $j = 1, \ldots, N_b$, are given by

$$\phi_i(\mathbf{x}_{b,j}, t) = \begin{cases} 1 & j = i, \\ 0 & \text{otherwise} \end{cases} \tag{4}$$

This implies that the scalar ϕ_i will evolve within the domain only due to inflow from boundary i given that the scalar value at other boundaries is set to zero. Four tracers are used to compute fate of water entering one of $N_b = 4$ channels corresponding to the MOK, GES, NMR, or SMR rivers. The fractional composition of the water in each cell due to inflow from one of the four boundaries can then be computed via mass transport coefficients.

Mass Transport Coefficients

Scalar transport through the junction can be described in terms of the fate, or mass fractional transport, for the proportion of tracer conveyed from an inlet channel i to an outlet channel j, namely

$$f_{i,j} = \frac{F^+_{i,j}}{F_{\text{out}}} \tag{5}$$

where $F^+_{i,j}$ = total flux of mass i out of the domain at channel j; and F_{out} = total mass leaving the domain over all outflows. A simplified description can also be derived by assuming complete mixing in the junction, which is similar to that of DSM2, e.g.

$$\tilde{f}_{i,j} = \frac{Q^+_j}{Q_{\text{out}}} \tag{6}$$

where $Q_{\text{out}} = \sum_{l=1}^{N_b} Q^+_l$. The tilde implies complete mixing where the mass flux is directly proportional to the outflow through j, i.e., Q^+_j, normalized by the total outflow. A full derivation of these mass transport coefficients is given in Appendix I.

Assessing Impacts of Modeling Assumptions on Mass Fraction Coefficients

The sensitivity of intrajunction dispersion to different flow features is evaluated by direct comparisons of different scenarios to the junction-scale base case on the 6-m grid. Each of the scenarios illustrates the relative impact incurred by a modeling assumption on the accuracy of the simulated mixing. To quantify the effect of each scenario, comparisons of instantaneous $f_{i,j}$ from Eq. (5) are computed using data from each scenario and the base case to test the sensitivity of $f_{i,j}$ to a particular modeling assumption. The difference is most simply quantified via the coefficient of determination r^2 between the base case X_{base} and each scenario X_{scn}. Definitions of r^2 are given in introductory statistics manuals (Corw et al. 1960; Navidi 2006). A coefficient of 1 implies that the modeling assumption does not impact computed $f_{i,j}$, whereas a

coefficient value of zero implies a strong effect of the particular modeling assumption. The statistical significance of r^2 depends on the number of degrees of freedom. For the data sets presented there are a minimum of 6 degrees of freedom because flow is correlated to advective flushing of the system, which occurs faster than 6 h over the two-day simulation periods. Statistical significance is obtained for $r^2 \geq 0.696$ at the 99% significance level (Crow et al. 1960).

A more-sensitive metric is the Murphy and Epstein (1989) skill score (SS), which is related to the coefficient of determination (r^2) (Murphy 1988; Ralston et al. 2010) by

$$SS = r^2 - \left(r - \frac{\sigma_{\text{scn}}}{\sigma_{\text{base}}}\right)^2 - \left(\frac{\overline{X_{\text{scn}}} - \overline{X_{\text{base}}}}{\sigma_{\text{base}}}\right)^2 \tag{7}$$

Interpretation of the SS is not as straightforward as for the coefficient of determination r^2, which represents the percentage variance captured by a scenario relative to the base case and ranges between -1 and 1. However, the SS is a more sensitive measure where poor agreement is indicated by a low or even negative value. Perfect agreement is quantified by $SS = 1$. Statistical significance is determined using the statistical significance for r^2 as a proxy. The SS is used to quantify scenario and base differences to evaluate the impact of grid resolution, three-dimensionality, the role of intrajunction flow features, and the assumption of complete mixing with a flow-weighted scheme similar to DSM2.

The impact of grid resolution on computation of $f_{i,j}$ is assessed by comparing simulations performed on a refined and coarse grid with 3- and 12-m horizontal resolution, respectively. These resolutions are compared to the base case grid with 6-m horizontal resolution. Although the assumption of weak stratification is suitable for the junction, three-dimensional features of the flow such as vertical shear layers or secondary circulation can impact tracer transport. Two-dimensional simulations are consequently used to evaluate the impact of three-dimensionality on the dispersion. These simulations are performed on the same 6-m grid as the base case using the same bathymetry, but with just one vertical layer. All other parameters are the same except the depth-averaged bottom drag in Eq. (2).

The importance of intrajunction flow features on mixing can be further quantified by comparing the base case to a linearized, hydrostatic, highly-viscous case, hereafter the Reduced Reynolds number (RRN) case, which fails to resolve the intrajunction flow features. Comparison of this case to the base case directly demonstrates the relative importance of high-Reynolds-number effects such as separation, secondary flows, and shear layer instability on model results for $f_{i,j}$. To eliminate high-Reynolds-number effects, the horizontal diffusion coefficient is set to $\nu_H = 1\ \text{m}^2\ \text{s}^{-1}$ and momentum advection and the nonhydrostatic pressure are ignored.

Even simpler approximations are used in standard engineering practice for practical modeling efforts such as the simple node-channel DSM2. For example, DSM2 assumes that mass is instantaneously and completely mixed at junctions. A particle entering a junction through one channel will exit immediately through another corresponding to the fractional volume outflow through that channel (CA DWR 1998; Kimmerer and Nobriga 2008). Thus, the junction is modeled as a single control volume in the node-channel framework. The appropriateness of this simple flow-weighting scheme that is used in models like DSM2 is evaluated by comparing $f_{i,j}$ [Eq. (5)] from the base case to the flow-weighted values $\tilde{f}_{i,j}$ [Eq. (6)] computed with the flow rates from the base case.

Results

Discharge, Stage, and Flow Validation

The model discharge at MOK on the regional-scale grid indicates the accuracy of the computed discharge in the system because USGS discharge measurements are used to force the regional-scale grid upstream at stations GES, NMR, SMR, and LPS, and a USGS stage measurement is imposed downstream at MOK. Reasonable flow rates are computed through the Georgiana Slough Junction at MOK [time series shown in Gleichauf et al. (2014)] with a Murphy and Epstein (1989) skill score of 0.91, where 1 is perfect agreement between model and observations. The stage is also well represented in the junction [time series shown in Gleichauf et al. (2014)] with a mean skill score of 0.95.

Observed and modeled depth-averaged streamwise flows corresponding to the regional-scale domain are compared in Fig. 2. Comparisons are best for interchannel flows with worse agreement for flows near the scour hole at the confluence of the GES and MOK rivers, as demonstrated by comparisons at GES and C. The flow above the scour hole at C is strongly three-dimensional and turbulent and the negative skill score indicates very poor agreement between the observation and depth-averaged model as anticipated because a depth-averaged model cannot accurately reproduce scour hole dynamics. Away from the scour hole, the overall depth-averaged streamwise flows are well represented.

The regional-scale flow is used to force the junction-scale domain with discharge boundary conditions applied in the GES, NMR, and SMR channels and a stage boundary condition applied in the MOK channel. Different flow conditions occur due to changes in forcing when the DCC is open and closed. Flow conditions when the DCC is open are represented by the two-day period between the start of June 1, 2012, and the end of June 2, 2012 (year-days 152 and 153). The two-day period beginning

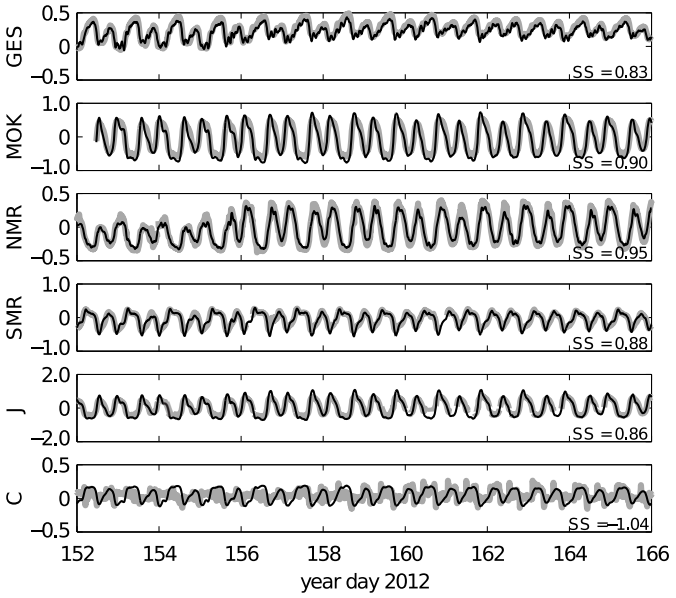

Fig. 2. Comparison of observed (gray) depth-averaged streamwise flow (m s^{-1}) to 2D SUNTANS predictions (black) on the regional-scale grid using ADCP measurements at GES, MOK, NMR, SMR, J, and C; Murphy and Epstein (1989) skill scores are also reported for the period of record shown; results are complementary to the 3D depth-averaged comparison in Gleichauf et al. (2014)

on June 9, 2012, and ending on June 10, 2012 (year-days 160 and 161), is representative of conditions when the DCC is closed. Quantitative comparisons for these periods are made to demonstrate model robustness. Discharge within the junction-scale domain (not shown) is very well represented with skill scores of 0.99 and 0.97 when the DCC is open and closed, respectively. Furthermore, agreement between the depth-averaged flow and ADCP observations (not shown) is reasonable at J and is 0.90 and 0.71 when the DCC is open and closed, respectively. The poor skill score obtained when the DCC is closed is attributable to a poor comparison caused by gaps within the ADCP record. Likewise, skill scores for depth-averaged flow and ADCP observations (not shown) at C (0.25 when the DCC is both open and closed) indicate that the flow is not accurately modeled and is perhaps the most revealing validation metric because it illustrates the limitations of standard practice in estuarine modeling.

The model does not reproduce the flow at C because of insufficient resolution to resolve the highly unsteady and separated flow dynamics within the scour hole. In addition to more resolution, three-dimensional RANS turbulence modeling may lead to improvement over restricting the parameterization to the vertical turbulent eddy-viscosity, as is standard practice in field-scale environmental flow modeling (e.g., Warner et al. 2005). However, RANS modeling is known to be poor at resolving separated flow dynamics, and hence large-eddy simulation (LES) may be needed along with submeter grid resolution. LES is certainly outside the realm of current estuarine modeling and falls outside the scope of this study which is designed to evaluate the importance of assumptions commonly made in practical engineering estuarine studies of the Delta.

The vertical structure of the horizontal velocity in regions of the junction that are not highly dependent upon resolution of the turbulent flow, e.g., locations away from the scour hole, are well represented by the 3D model. For example, the predicted vertical variability for velocity at the NMR location using a three-dimensional simulation on the regional-scale domain is compared to observations in Fig. 3. Agreement between model and ADCP streamwise flows is quite reasonable as shown in Figs. 3(a and c). The transverse eddy observed in the ADCP observations, the currents of which are one order of magnitude smaller than those for the streamwise flow, is likewise observed in the model predictions in Figs. 3(b and d), although the simulated flow is smoother because turbulence is parameterized and not explicitly resolved. Additional comparisons to drifter observations in Gleichauf et al. (2014) demonstrate capability of the model to reproduce the large-scale structure of the flow, particularly for the eddy formed at the confluence of GES and MOK above the scour hole at ADCP C.

Tidal River Flow Features

Results from the numerical model and field study (Gleichauf et al. 2014) are used to identify and characterize intrajunction flow features occurring within GSJ over ebb and flood tides, schematically illustrated in Figs. 1(d and e). Separation zones and shear layers form at the confluence of Georgiana Slough (GES) with the combined flow of the Northern and Southern Mokelumne Rivers (NMR and SMR, respectively) during ebb tide [Fig. 1(d)]. A shear layer also forms between NMR- and SMR-sourced waters. A separation eddy and upwelling zone periodically form due to the strong curvature at the western headland of the junction.

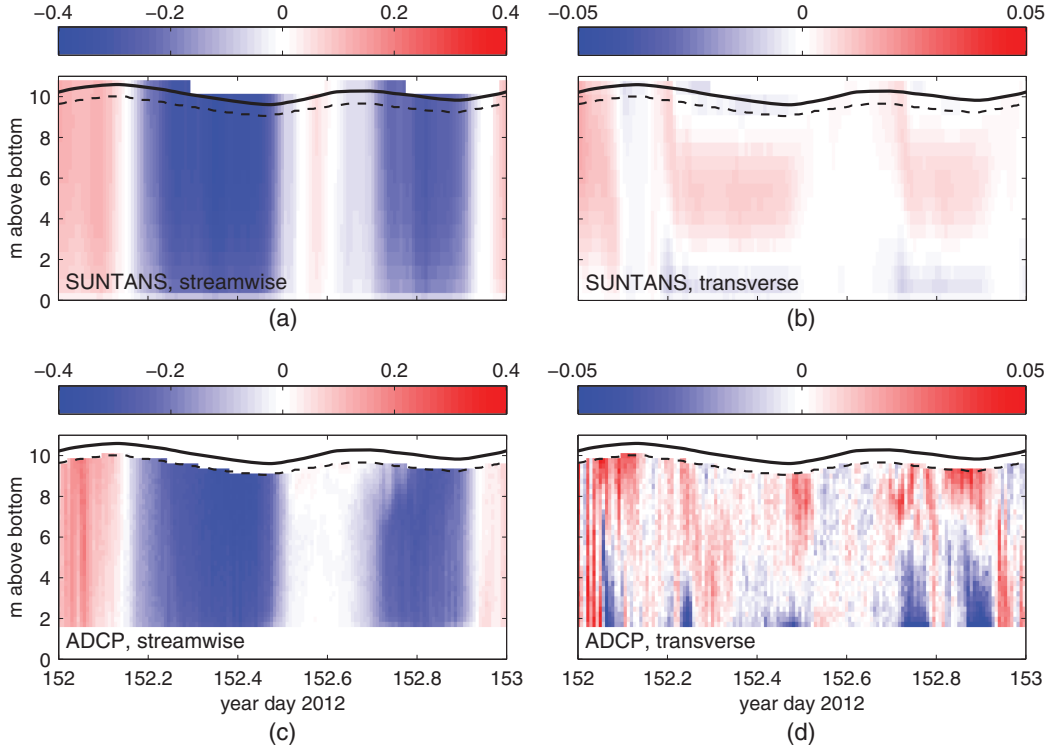

Fig. 3. (Color) Comparison of 10-min filtered velocities at NMR on the base case junction-scale quadrilateral C-grid with 6-m horizontal resolution for (a) SUNTANS streamwise flow u_s; (b) SUNTANS transverse flow u_t; (c) ADCP streamwise flow u_s; (d) ADCP transverse flow u_t; all units are in m s^{-1}; black line designates the predicted free surface and the dashed line indicates the upper limit of reliable ADCP observations; ADCP does not measure flow near the bed or free surface; data for a single day are shown to illustrate agreement in vertical structure between SUNTANS results and ADCP observations

On flood tide [Fig. 1(e)], a transient turbulent jet and its accompanying separation zones are formed at the confluence of GES and the junction. The shear layer formed by GES-sourced and MOK-sourced waters extends into NMR. Flows originating from MOK separate into both NMR and SMR, with transient separation at the eastern headland of the junction. The flow is shallow and largely two-dimensional, except for localized regions near the western and eastern junctions, as illustrated in Figs. 1(d and e). The timing, strength, and impact of these flow features is driven by DCC gate operations.

Delta Cross-Channel Gate Operations

DCC gate operations have a substantial impact on the relative strength of the river flows (mean) compared to the tidal flows (oscillatory deviation from mean), and hence DCC operations are particularly important contributors to dispersion. A measure of the relative strength of river and tidal forcing is obtained using a 25-h low pass filter, denoted by $<\cdot>$. A useful metric is the ratio $\mathcal{R}$ of the tidally filtered riverine flow, $\langle Q \rangle$, to the root-mean square of the residual $Q - \langle Q \rangle$, which is a proxy for the tidal flow discharge component (Gleichauf et al. 2014)

$$\mathcal{R} = \frac{\langle Q \rangle}{\sqrt{2\langle (Q - \langle Q \rangle)^2 \rangle}} \tag{8}$$

A value of 1 indicates nearly equal strength between the river and tidal flow constituents. Values less than 1 indicate tidal dominance of flows (Gleichauf et al. 2014). The impact of closing the DCC gate at 5:00 p.m. on June 4, 2012, (year-day 155) is shown in Fig. 4. After the abrupt closure, the system responds to the change in conditions over a one day period. Representative periods when the DCC is open (year-days 152 and 153) and closed (year-days 160 and 161) are highlighted by the blue (DCC open) and green (DCC closed) shaded regions in Fig. 4, which uses flows derived from the regional-scale triangular C-grid model.

In general, the system is more tidally influenced when the DCC is closed. DCC closed flow conditions result in the junction acting as a diffluence (inflow split into two or more outflows) more frequently (47%) than for DCC open conditions (32%). The junction acts as a confluence with multiple inflows flowing into a single outflow during the remainder of the time. Therefore, the junction is expected to have increased dispersion when the DCC is closed because of a higher likelihood that flows within the junction split into separate masses. For example, when the DCC gate is open, flows in GES and NMR are more strongly driven by downstream river flows. On the other hand, when the DCC gate is closed, GES river flows are more dominant and NMR becomes nearly tidal. In contrast to GES and NMR river flows, SMR and MOK are both primarily tidally forced for both periods.

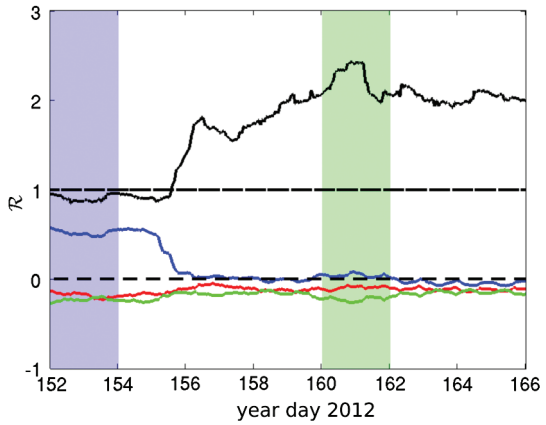

Fig. 4. (Color) Tidally filtered ratio of riverine to tidal flow discharge $\mathcal{R}$ for each channel connected to the Georgiana Slough Junction: GES (black), NMR (blue), SMR (red), and MOK (green); positive values correspond to flow entering the junction and negative values to flow leaving the junction; blue shaded region corresponds to the period June 1–3, 2012 (DCC open), and the green shaded region the period June 9–11, 2012 (DCC closed)

Mass Fraction Coefficients

An example of instantaneous mass fraction coefficients $f_{i,j}$ for $i =$ GES, computed with the base case junction-scale grid, is shown in Fig. 5. The figure depicts the fate of mass flowing into the junction from GES. Colored shading in the plots indicates how the GES inflow is partitioned among the other three outflows as well as back to GES itself. Fig. 5(a) depicts the mass fraction coefficients when the DCC is open while Fig. 5(b) depicts them when the DCC is closed. For each case, the tracer field is initialized to $1/N_b$ at $t_0 =$ 00:00 June 1, 2012 (DCC open; June 1–3, 2012), and $t_0 =$ 00:00 June 9, 2012 (DCC closed; June 9–11, 2012), corresponding to the start of the simulations assuming even mixing within the domain. The initial scalar field is readily forgotten because of strong advective flushing within half a tidal cycle.

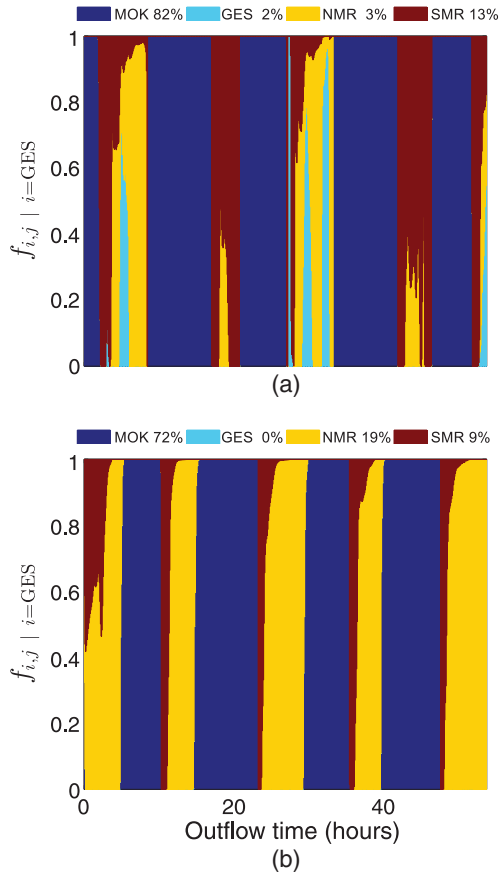

Fig. 5. (Color) Time-varying mass fraction coefficient $f_{i,j}$ for GES inflow, i = GES, with (a) DCC gate open (June 1–3, 2012); (b) DCC gate closed (June 9–11, 2012); the legend for each figure indicates the total time-averaged fractional transport (time-averaged $f_{i,j}$) over the time period with respect to each outflow channel

For example, at time $t = 0$ h corresponding to ebb tide in Fig. 5(a), all of the GES water flows out of MOK. However, at time $t = 30$ h during flood tide, water flows out of GES, NMR, and SMR. Fig. 5(a) (open DCC) is characterized by reduced, time-averaged, NMR inflow (3 versus 19%) as compared to when the DCC is closed. Consequently, waters entering the junction from GES return to and flow out to GES only when the DCC is open [Fig. 5(a)].

The mass fraction is forced by the tidal signal corresponding to ebb and flood tides. However, when river flows are much greater than tidal flows, as is the case when the DCC is open, $f_{i,j}$ is more variable with respect to a particular inflow than when the DCC is closed because there is stronger riverine forcing. For example, when the DCC is open [Fig. 5(a)] there is a marginal amount of water that returns to GES and a larger portion of the flow (13 versus 9%) on flood tides leaves via SMR as compared to when the DCC is closed [Fig. 5(b)]. Time-averaged $f_{i,j}$ values corresponding to each time period are noted in the legend, indicating the bulk fate over the time period. For example, the fraction of water exiting MOK during ebb tide is reduced from 82 to 72% time-averaged $f_{i,j}$, corresponding to increased tidal influence when the DCC is closed. Thus, 10% of the mass entering channel i and leaving channel j is rerouted. As demonstrated, the detail of information provided by $f_{i,j}$ is substantial and quantifies the intrajunction transport occurring in the junction.

Modeling Assumption Assessment

An integrative assessment of modeling assumptions as quantified by $f_{i,j}$ is performed for each modeling scenario relative to the base case using the *SS* (Fig. 6). Each skill score number indicates the ability of the model scenario to simulate transport for flows from one channel to another, including mixing, relative to the base case. Holistically, results above 0.95 indicate strong agreement, results above 0.90 indicate good agreement, and results below 0.80 indicate poor agreement. Descriptive statistics over all inflow–outflow pairs broadly indicate the validity of each modeling scenario relative to the base case.

Discussion

Effects of Grid Resolution

Dispersion primarily depends on flow-phasing within the junction and not on resolving three-dimensional flow features, as indicated by the results in Figs. 6(a and b), which present *SS* values computed between the fine-grid and coarse-grid simulations and the base case, respectively. These results show that the mass fraction coefficients are very well represented for both cases when the DCC is open and closed, with mean and RMS *SS* values between 0.97 and

$f_{i,j}$ flow	a. *3mV6m*		b. *6mV12m*		c. *2dV3d*		d. *RRN*		e. *FW*	
	O	C	O	C	O	C	O	C	O	C
1. M2M	**0.92**	***0.85***	**0.87**	***0.68***	**0.77**	***0.53***	**0.92**	***0.72***	0.51	0.52
2. M2G	**0.97**	–	**0.96**	–	**0.63**	–	**0.91**	–		–
3. M2N	**0.97**	**0.98**	**0.92**	**0.95**	**0.89**	**0.91**	**0.93**	**0.98**	**0.94**	**0.92**
4. M2S	**0.96**	**0.98**	**0.95**	**0.97**	**0.89**	**0.92**	**0.99**	**1.00**	**0.37**	*-0.1*
5. G2M	**1.00**	**0.99**	**0.98**	**0.99**	**0.99**	**0.99**	**0.97**	**0.99**	**0.72**	**0.75**
6. G2G	**1.00**	–	**1.00**	–	**0.99**	–	**1.00**	–	**0.06**	–
7. G2N	**0.98**	**0.99**	**0.96**	**0.99**	**0.89**	**0.96**	0.53	**0.88**	0.32	**0.66**
8. G2S	**1.00**	**1.00**	**0.98**	**0.98**	**0.99**	**0.99**	**0.80**	**0.88**	0.37	-0.0
9. N2M	**1.00**	**1.00**	**1.00**	**0.99**	**1.00**	**0.99**	**0.99**	**0.99**	**0.78**	**0.90**
10. N2G	**1.00**	–	**0.90**	–	**0.68**	–	–	–	0.59	–
11. N2N	**0.99**	**0.99**	**0.98**	**0.99**	**0.95**	**0.93**	**0.77**	**0.95**	**0.14**	**0.66**
12. N2S	**1.00**	**1.00**	**1.00**	**1.00**	**1.00**	**1.00**	**0.99**	**0.98**	0.39	0.57
13. S2M	**1.00**	**1.00**	**1.00**	**1.00**	**0.99**	**0.99**	**1.00**	**0.99**	**0.73**	**0.80**
14. S2G	***0.76***	–	***0.36***	–	***-0.4***	–	–	–	0.46	–
15. S2N	**0.96**	**1.00**	**0.94**	**0.99**	**0.98**	**0.99**	*0.45*	**0.98**	***0.28***	**0.64**
16. S2S	**1.00**	**1.00**	**0.99**	**1.00**	**0.99**	**0.99**	**0.96**	**0.97**	0.60	0.67
Mean	**0.97**	**0.98**	**0.92**	**0.96**	**0.83**	**0.93**	**0.87**	**0.94**	0.48	**0.57**
RMS	**0.97**	**0.98**	**0.93**	**0.96**	**0.89**	**0.94**	**0.89**	**0.95**	0.54	**0.66**
Max	**1.00**	**1.00**	**1.00**	**1.00**	**1.00**	**1.00**	**1.00**	**1.00**	**0.94**	**0.92**
Min	**0.76**	**0.85**	**0.36**	**0.68**	**-0.4**	**0.53**	0.45	**0.72**	0.06	-0.1
Std Dev	**0.06**	**0.04**	**0.15**	**0.08**	**0.33**	**0.13**	**0.17**	**0.08**	**0.24**	**0.33**

Fig. 6. *SS* skill-scores comparing $f_{i,j}$ mass fraction coefficients for each column: (a) the 3 mV6 m [base (6 m) versus fine (3 m)], column; (b) the 6 mV12 m [base (6 m) versus coarse (12 m)], column; (c) 2dV3d [base (3D) versus 2D], column; (d) RRN (base versus reduced-Reynolds-number linearized, viscous flow); (e) FW [base (3D) versus flow-weighted 0D $\tilde{f}_{i,j}$]; periods when DCC is open (June 1–3, 2012) and closed (June 9–11, 2012) are denoted by O and C, respectively; dashed values of *SS* indicate there is no flow into GES and omitted values indicate an exceptionally poor *SS*; sketches indicate flow pathways; italicized values indicate the smallest values in each column; values with a 99% or greater significance level are designated by bold, letters M, G, N, and S denote the Mokelumne, Georgiana Slough, North Mokelumne, and South Mokelumne Rivers, respectively with M2M indicating $f_{i,j}$ for flow from the Mokelumne River into the Mokelumne river, for example

J. Hydraul. Eng., 2016, 142(8): 04016019

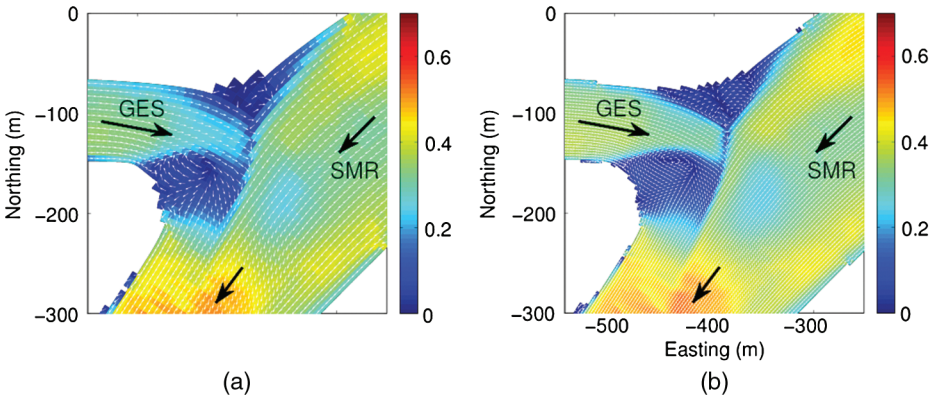

Fig. 7. (Color) Comparison of normalized surface flow vectors, shown in white, and current magnitudes, shown in color, for (a) base case with 6-m resolution; (b) refined case with 3-m resolution; snapshot is during ebb tide at 9:00 p.m. on June 2, 2012, when the DCC is open and flow is from SMR into GES

0.98, indicating that there is sufficient resolution on a 6-m grid to resolve the large-scale flow features most important for dispersion. Some fidelity is lost for the coarser resolution of 12 m as indicated by the reduced minimum and the reduction of mean and RMS SS by approximately 0.02. The most significant impact of grid resolution is found for flow from SMR into GES when the DCC is open (Row 14, $SS = 0.76$ for the fine case and $SS = 0.36$ for the coarse case) and MOK into MOK when the DCC is closed (Row 1, $SS = 0.68$). Grid resolution affects $f_{i,j}$ for flows from SMR into GES because of the existence of a resolution dependent recirculating eddy (Fig. 7). In Fig. 7(a), the eddy is only partially resolved in the base case and its core, as observable in Fig. 7(b), is indistinct due to lack of resolution on the 6-m grid. The eddy is increasingly poorly resolved at lower resolutions, e.g., as quantified by $SS = 0.36$ for the 12-m grid. Additionally, the recirculation at the northern bank of the confluence of GES with the junction requires finer resolution in order to be well-resolved. However, large-scale features, such as the jet originating from GES, are computed reasonably well with the 6-m base case, even if the precise location of upwelling varies between the cases.

The GSJ flow is challenging to simulate because it depends upon computed scour hole dynamics. However, the coarse 6-m model captures $\geq 90\%$ of the variance in $f_{i,j}$ when compared to the fine 3-m model (mean $SS = 0.97$). Thus, $f_{i,j}$ is overall well-represented by use of the coarser model in spite of neglecting details of the recirculating flow at the GES and MOK junction at the scour hole, suggesting that in general, higher resolution is not necessary to obtain reasonable estimates for tidally averaged dispersion at the junction.

Two-Dimensional versus Three-Dimensional Simulation

The flow in GSJ is well-mixed and the channel aspect ratio is small in most of the junction, indicating that vertical accelerations are largely negligible, except at the scour hole. This implies that the flow will be predominantly hydrostatic and suggests that a two-dimensional approximation is reasonable. As indicated in Fig. 6(c), mass fraction coefficients computed with a 2D model often show good agreement, suggesting that in general, 2D simulations are sufficient to resolve dominant intrajunction dispersion processes for many inflow–outflow combinations. However, intrajunction flow features such as the eddy and jet at the scour hole, separation zones near the western confluence of GES and MOK and eastern confluence of NMR and SMR, and junction shear layers are intermittent in time and only partially simulated by a 2D model. Flows traversing the scour hole are of course impacted by use of a 2D model, as shown by the poor agreement in Rows 1, 2, 7, 10, and 14 of Fig. 6(c).

For strongly tidal flows, the return flow from MOK into MOK (Row 1, DCC closed) is poorly represented ($SS = 0.53$) by the 2D model because of the scour hole located at the confluence of GES and the junction, as shown in Fig. 8. A fully 3D flow is required to

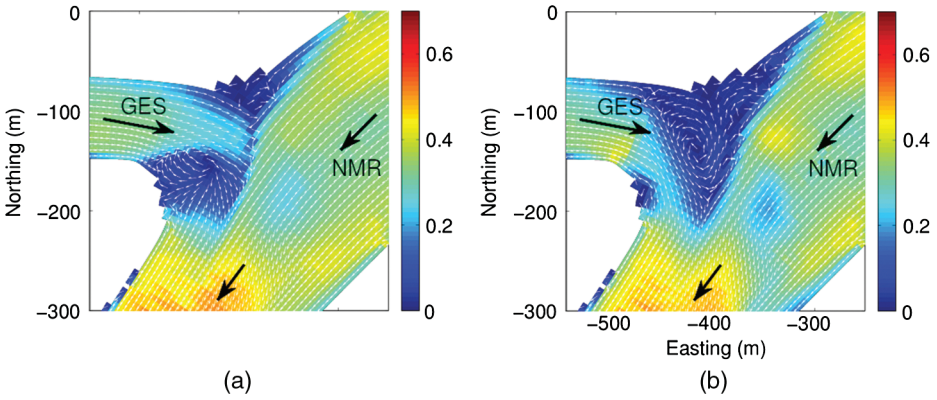

Fig. 8. (Color) Comparison of normalized surface flow vectors, shown in white, and current magnitudes, shown in color, for (a) 3D base case; (b) 2D case when the DCC is open during ebb tide at 9:00 p.m. on June 2, 2012; the comparison highlights scour hole dynamics at the confluence of the GES river with the junction

simulate the recirculation at the western bank of the confluence of GES with the junction main channel. Use of a 2D approximation artificially enhances the importance of horizontal shear in development of recirculation zones by completely neglecting the importance of vertical recirculation at the scour hole, which is known to be important (Best and Roy 1991). Consequently, a 2D simulation fails to appropriately account for $f_{i,j}$ if flow from channel i into channel j encounters rapidly varying bathymetric features such as a scour hole, as shown in Rows 2, 7, 10, and 14 of Fig. 6(c) (e.g., $SS = 0.63$). Likewise, flows into GES are also impacted and have low SS. Strong separation at the GES and MOK confluence further increases the discrepancy between 2D and 3D simulations because of overprediction of the strength of separated flows by the 2D model, as demonstrated by larger eddies in the 2D simulation in Fig. 8(b) as compared with the 3D base case simulation in Fig. 8(a).

In spite of these complications, the remainder of the cases in Fig. 6(c) have $SS \geq 0.90$, indicating that the 2D model captures at least 90% of the variance obtained via the 3D model except for flows traversing the scour hole. If bathymetry varies slowly and there is no separation zone along the flow path, as is the case for other channels such as MOK flowing into NMR and SMR (Rows 3 and 4), results obtained by the 2D model well-approximate the 3D model because of the lack of curvature and strongly hydrostatic nature of the flow within the main channel of the junction. The mean and RMS SS range from 0.83 to 0.94 and on average the 2D model replicates 84% of the variability in $f_{i,j}$ compared with the 3D model, with the exceptions noted earlier. Thus, the use of a 2D model may be appropriate when the flow is unstratified, there is minimal channel curvature, and the river is much wider than it is deep. However, for transport traversing intrajunction flow features or in the larger Delta system, these conditions may not met, and a fully 3D model will be necessary to accurately simulate dispersion over subtidal timescales.

Effect of Intrajunction Flow Features

The RRN case simulates mass transport in the laminar regime in absence of flow separation, eliminating the intrajunction flow features suspected to dominate intrajunction mixing. Fig. 6(d) therefore presents SS values quantifying the relative importance of intrajunction flow features on mixing. Flows into and from NMR and GES are most impacted by ignoring the effect of the localized flow features on the mass fraction coefficient. The most significant differences between the base case and the RRN case are obtained for flow of GES into NMR and flow from SMR into NMR when the DCC is open, shown by Rows 7 and 15 in Fig. 6(d) ($SS = 0.53$ and 0.45). Flow from GES into NMR occurs less than 21% of the time and flow from SMR into NMR occurs less than 1% of the time and for all flow conditions. These flow pathways (GES into NMR and SMR into NMR) are located directly near the western and eastern secondary flow features. The flows traverse complex intrajunction flow features such as recirculation zones, which are not captured by the RRN model. Accuracy of the simulated dispersion is consequently poor.

Although the recirculation regions are poorly represented by the highly viscous RRN case, most flows have reasonable agreement [Fig. 6(d)]. This indicates that failure to account for the high-Reynolds-number flow features within the junction will only be a problem if overall dispersion in the junction is sensitive to resolution of an intrajunction flow feature that strongly impacts the mass fraction. For example, if the junction dispersion is strongly dependent upon flow pathways from GES into NMR and SMR into NMR (Rows 7 and 15), a model capable of resolving secondary flow features of the scour hole at the confluence of GES and the junction as well as the eastern headland at the SMR and NMR confluence would be necessary. However, given that these flow conditions account for less than 21% of the total flow, the dispersive contributions of this flow pathway are expected to be moderately important because the flow is advection dominated.

Effect of the Flow-Weighted Mixing Scheme

Based on the results of the previous modeling scenarios, one would expect a lowest-order parameterization of mixing to be inadequate. As expected, the average agreement between $\tilde{f}_{i,j}$ and $f_{i,j}$ [shown in Fig. 6(e)] is poor with skill scores of 0.48 and 0.57 for the DCC open and closed, respectively. Minimum SS of 0.06 and −0.1 are also obtained.

In general, mass fraction coefficients computed with the base case are typically smaller than the DSM2 modeled mass fraction coefficients due to the assumption of complete and instantaneous mixing within the junction when computing $\tilde{f}_{i,j}$. Consequently, there is less intrajunction mixing for the base case, resulting in larger scalar variance relative to DSM2. The larger scalar variance is accompanied by larger peak concentrations because the peaks are not necessarily diluted within the junction, as is the case for complete and instantaneous mixing.

The best agreement between the base case and the flow-weighted mixing scheme is found for flow from MOK into NMR (SS of 0.94 and 0.92 for the DCC open and closed, respectively). The predominant flow feature along this flow path is the shear layer in the middle of the junction, and mixing across this shear layer is secondary when compared to the effect of transport by the splitting diffluence flow. However, for flow from MOK into GES, with a flow path that traverses the scour hole and its complex associated secondary flow features, agreement is poor with a strong negative SS that is excluded as an outlier in the descriptive statistics computed for the DCC open case. Diffluent flows, such as from GES into NMR ($SS = 0.32$) and GES into SMR ($SS = 0.37$) are poorly represented and insignificant at the 95% confidence level.

These results suggest that simple DSM2 flow-weighted mass fractions are insufficient to represent mixing at the junction because they cannot represent the secondary flow features and inadequately parameterize transport under diffluent flows. Agreement between $f_{i,j}$ for the base case and flow-weighted $\tilde{f}_{i,j}$ is typically poor for flows from and into GES, with the exception of there being no inflows into GES when the DCC is closed. For these trivial cases, there is perfect agreement between $f_{i,j}$ and $\tilde{f}_{i,j}$, giving a value of $SS = 1$, which is designated with horizontal lines in Fig. 6. Similarly, flows into SMR are not well represented by the DSM2 flow-weighted model. These discrepancies are attributable to failure of the flow-weighted model to account for trapping in the eddies or in separation zones near the GES-junction confluence. The flow-weighted model also overpredicts mixing across the junction shear layer because it assumes complete mixing within the junction.

Conclusions

The most important factor influencing scalar fate within a channel junction is the relative difference between flows through channels connected to the junction. For simplified models such as DSM2, neglecting specific flow pathways results in reduced accuracy when compared to models that resolve, at a minimum, the two-dimensional horizontal intrajunction flows. Mass transfer fate can

be well-represented in large parts of the flow without necessarily resolving small-scale intrajunction flow features because they are highly localized in both space and time. However, secondary flow features modify transfer of mass from one channel to another and may be very important to quantify local intrajunction mixing. For example, the horizontal recirculation eddy near the GES and MOK confluence may serve to entrain fluid and form a transient dead zone. Secondary flow features may only affect a small amount of the total discharge through the junction, but they are important for local intrajunction dispersion. It is possible that they play a more-dominant role in other junctions characterized by strong secondary circulation because secondary circulation due to bends enhances transverse mixing that, when accompanied by strong transverse gradients in the flow, can lead to enhanced longitudinal mixing (Fischer 1973).

A coarse 2D model provides much better estimates of scalar transport through the junction when compared to the node and link DSM2 model. Although high-resolution 3D modeling would no doubt resolve more fine-scale mixing processes not resolved by the 2D model, the tidally averaged dispersion in the junction appears to be only moderately sensitive to small-scale 3D flow features for this unstratified flow. In part, this is because the 3D flow features are intermittent in time relative to advection over the dominant tidal time scale. Furthermore, because the main channel junction is relatively straight and the flow is largely hydrostatic, secondary flow features arising from channel flow curvature are weak. Therefore, the present study is unable to ascertain the role of mixing in junctions with strong curvature, particularly in the presence of stratification (Kalkwijk and Booij 1986; Lacy and Monismith 2001; Nidzieko et al. 2009). Dispersion inferences from study of the stratified, tidally-influenced, curved Elkhorn Slough near Monterey Bay, California highlight the complexity of this problem and may be indicative for other locations (Nidzieko et al. 2009).

Supertidal intrajunction flow features only moderately affect mixing at the GSJ junction. The combined effect of tidal-scale oscillations superimposed on subtidal flows is the dominant driver of dispersion because tidal oscillations lead to more-frequent flow splittings at diffluences, which cause splitting of individual tracer patches within the junction (Gleichauf et al. 2014; Wolfram 2013). Such splitting is likely the cause of the strong scale-dependent dispersion ($K \approx 1{,}000\ \mathrm{m^2\ s^{-1}}$) estimated for mixing in the junction network that constitutes the Delta (Monismith et al. 2009). Because the 2D model captures a substantial portion of the variability inherent in $f_{i,j}$, it is likely that it will better reproduce system-wide dispersion in the junction network than the simpler DSM2 approach. However, it is left to a future study to ascertain the role of 2D versus 3D simulation for the entire Delta system, which includes more-complex dispersion processes due to the interactions between strong curvature, stratified flows, and channel junctions.

Intrajunction flow features affect localized mixing, as illustrated by low values of *SS* arising when flows traverse the scour hole and its horizontal recirculating eddy. However, small-scale intrajunction flow features only substantially affect mixing over relatively short spatio-temporal scales. In GSJ the bulk junction-scale mixing is only moderately sensitive to these features because they are highly sporadic in time and space. Consequently, simplified transport assumptions such as two-dimensionality and even a reduced-Reynolds-number approach can reasonably reproduce bulk intrajunction mixing for certain flow pathways in this simple junction. More-restrictive modeling assumptions, however, such as complete mixing as assumed in DSM2, cannot resolve the effects of bulk flow features arising from the confluent–diffluent tidal flow and hence are inappropriate to simulate mixing at channel junctions.

Appendix. Derivation of Mass Fractional Transport Coefficients

Mass fractional transport from an inlet channel i to an outlet channel j can be derived by considering the governing equation for the total mass in the junction entering boundary i, or M_i. Integrating the transport Eq. (3) over the three-dimensional junction domain gives

$$\frac{dM_i}{dt} + \sum_{j=1}^{N_b} F_{i,j} = 0 \tag{9}$$

where, as defined earlier, N_b = number of boundaries, and the flux of scalar entering inlet i and exiting outlet j is given by

$$F_{i,j}(t) = \int_{\mathbf{x}_{b,j}} \phi_i(\mathbf{x}, t)\mathbf{u} \cdot \mathbf{n} dA \tag{10}$$

where $\mathbf{n}$ = outward normal at the given boundary. Due to boundary conditions in Eq. (4), $F_{i,j}(t) = 0$ if $\mathbf{u} \cdot \mathbf{n} \le 0$ and $i \neq j$, implying no flux of scalar i enters the domain through any of the other boundaries. If Q_i is the flow rate through boundary i, then positive and negative superscripts can be used to imply outflows and inflows, such that $F^+_{i,j}(t) = F_{i,j}(t)$ when $Q_j \ge 0$ and $F^-_{i,j}(t) = F_{i,j}(t)$ when $Q_j < 0$. This implies that the inflow mass flux is given by

$$F^-_{i,j}(t) = \begin{cases} F_{\text{in}} = -|Q_i| & i = j \\ 0 & \text{otherwise} \end{cases} \tag{11}$$

Now, define the flux of mass through all outlets with positive outflow as

$$F_{\text{out}} = \sum_{j=1}^{N_b} F^+_{i,j} \tag{12}$$

Defining the ratio of mass i exiting the domain at boundary j to the total flux of mass i out of the domain as

$$f_{i,j} = \frac{F^+_{i,j}}{F_{\text{out}}} \tag{13}$$

The governing equation for the total mass in the domain is then given by

$$\frac{1}{F_{\text{out}}}\frac{dM_i}{dt} + \frac{F_{\text{in}}}{F_{\text{out}}} + \sum_{j=1}^{N_b} f_{i,j} = 0 \tag{14}$$

Under steady-state conditions, $dM_i/dt = 0$, which gives $F_{\text{in}} = -F_{\text{out}}$, so that

$$\sum_{j=1}^{N_b} f_{i,j} = 1 \tag{15}$$

assuming that $F_{\text{out}} \neq 0$. Eq. (15) is a statement of mass conservation in terms of $f_{i,j}$.

A simplified description of $f_{i,j}$ is given by assuming complete mixing in the junction, which is similar to that of the Delta Simulation Model 2 (DSM2). DSM2 assumes that mass is completely mixed at the junction and is instantaneously transported

through the junction corresponding to the fractional outflow (CA DWR 1998; Kimmerer and Nobriga 2008). Assuming complete mixing within the domain, the mass fluxes are given by $F^+_{i,j}(t) = \phi_i Q^+_j$, which implies a mass conservation equation of the form

$$\frac{d}{dt}(\phi_i V) + Q^-_i + \phi_i \sum_{j=1}^{N_b} Q^+_j = 0 \tag{16}$$

where V = volume of the domain. Assuming steady flow yields

$$Q^-_i + \phi_i \sum_{j=1}^{N_b} Q^+_j = 0 \tag{17}$$

which implies a steady-state concentration within the domain of

$$\tilde{\phi}_i = -\frac{Q^-_i}{\sum_{j=1}^{N_b} Q^+_j} \tag{18}$$

and a mass fraction coefficient of

$$\tilde{f}_{i,j} = \frac{Q^+_j}{\sum_{l=1}^{N_b} Q^+_l} \tag{19}$$

where the tilde implies steady flow and complete mixing, and, as with $f_{i,j}$, mass conservation implies $\sum_{j=1}^{N_b} \tilde{f}_{i,j} = 1$. Eq. (19) implies that, in the DSM2 model, mass is partitioned at a junction according to a simple flow weighting. Assuming that at any instant in time there is only one inflow through inlet i, then $\sum_{j=1}^{N_b} Q^+_j = -Q^-_i$, so that

$$\tilde{f}_{i,j} = -\frac{Q^+_j}{Q^-_i} \tag{20}$$

As an example, consider a confluence with inflow into Inlet 1 ($Q_1 < 0$) and outflow from Outlets 2 and 3 ($Q_2 > 0$ and $Q_3 > 0$ with $Q_2 + Q_3 = -Q_1$). Then, Eq. (19) implies $f_{12} = -Q_2/Q_1$ and $f_{13} = -Q_3/Q_1$.

Acknowledgments

Support for this research was provided by the Delta Science Program and by the Department of Defense through the National Defense Science & Engineering Graduate Fellowship (NDSEG) Program. Special thanks to Jon Burau and the USGS California Water Science Center team for their help in the field. USGS/DWR discharge, stage, and bathymetry data was generously provided by Patricia Orlando (USGS), Brad J Sullivan (USGS), Joel Dudas (DWR), and Wyatt Pearsall (DWR). Advice of EMFL colleagues Sean Vitousek, Bobby Arthur, Matt Rayson, Joel Weitzman, and Ed Gross was invaluable in conducting this study. The authors also thank two anonymous reviewers, an anonymous Associate Editor, and Chief Editor Prof. Thanos Papanicolaou whose comments greatly improved the quality of the manuscript.

References

Best, J., and Roy, A. (1991). "Mixing-layer distortion at the confluence of channels of different depth." *Nature*, 350(6317), 411–413.

Biron, P. M., Ramamurthy, A. S., and Han, S. (2004). "Three-dimensional numerical modeling of mixing at river confluences." *J. Hydraul. Eng.*, 10.1061/(ASCE)0733-9429(2004)130:3(243), 243–253.

Bradbrook, K., Lane, S., Richards, K., Biron, P., and Roy, A. (2001). "Role of bed discordance at asymmetrical river confluences." *J. Hydraul. Eng.*, 10.1061/(ASCE)0733-9429(2001)127:5(351), 351–368.

CA DWR (California Department of Water Resources) (1998). "Delta simulation model II-DSM2." ⟨http://baydeltaoffice.water.ca.gov/modeling/deltamodeling/models/dsm2/dsm2.cfm⟩ (Feb. 1, 2016).

CA DWR (California Department of Water Resources). (2012). "Methodology for flow and salinity estimates in the Sacramento-San Joaquin delta and Suisun Marsh." *Rep. No. 23rd Annual Progress Rep. to the State Water Resources Control Board*, Bay-Delta Office, Delta Modeling Section, Sacramento, CA.

Casulli, V., and Walters, R. (2000). "An unstructured grid, three-dimensional model based on the shallow water equations." *Int. J. Numer. Meth. Fluids*, 32(3), 331–348.

Casulli, V., and Zanolli, P. (2002). "Semi-implicit numerical modeling of nonhydrostatic free-surface flows for environmental problems." *Math. Comput. Modell.*, 36(9), 1131–1149.

Chua, V., and Fringer, O. (2011). "Sensitivity analysis of three-dimensional salinity simulations in North San Francisco Bay using the unstructured-grid SUNTANS model." *Ocean Modell.*, 39(3–4), 332–350.

Crow, E. L., Davis, F. A., and Maxfield, M. W. (1960). *Statistics manual*, Dover, New York.

Fischer, H. (1973). "Longitudinal dispersion and turbulent mixing in open-channel flow." *Annu. Rev. Fluid Mech.*, 5(1), 59–78.

Fringer, O., Gerritsen, M., and Street, R. (2006). "An unstructured-grid, finite-volume, nonhydrostatic, parallel coastal ocean simulator." *Ocean Modell.*, 14(3), 139–173.

Fringer, O. B. (2006). "SUNTANS source code." ⟨https://github.com/ofringer/suntans⟩ (Feb. 1, 2016).

Gleichauf, K., Wolfram, P., Monsen, N. E., Fringer, O., and Monismith, S. (2014). "Dispersion mechanisms of a tidal river junction in the Sacramento-San Joaquin delta, California." *San Francisco Estuary Watershed Sci.*, 12(1–23), in press.

Gross, E. S., Koseff, J. R., and Monismith, S. G. (1999). "Three-dimensional salinity simulations of South San Francisco Bay." *J. Hydraul. Eng.*, 10.1061/(ASCE)0733-9429(1999)125:11(1199), 1199–1209.

Kalkwijk, J., and Booij, R. (1986). "Adaptation of secondary flow in nearly-horizontal flow." *J. Hydraul. Res.*, 24(1), 19–37.

Kimmerer, W., and Nobriga, M. (2008). "Investigating particle transport and fate in the Sacramento-San Joaquin delta using a particle tracking model." *San Francisco Estuary Watershed Sci.*, 6(1), 1–26.

Lacy, J., and Monismith, S. (2001). "Secondary currents in a curved, stratified, estuarine channel." *J. Geophys. Res.*, 106(C12), 31283.

MacWilliams, M. L., Bever, A. J., Gross, E. S., Ketefian, G. S., and Kimmerer, W. J. (2015). "Three-dimensional modeling of hydro dynamics and salinity in the San Francisco estuary: An evaluation of model accuracy, X2, and the low-salinity zone." *San Francisco Estuary Watershed Sci.*, 13(1), 1–37.

Mellor, G. L., and Yamada, T. (1982). "Development of a turbulence closure model for geophysical fluid problems." *Rev. Geophys.*, 20(4), 851–875.

Monismith, S. G., et al. (2009). "Thermal variability in a tidal river." *Estuaries Coasts*, 32(1), 100–110.

Murphy, A., and Epstein, E. (1989). "Skill scores and correlation coefficients in model verification." *Mon. Weather Rev.*, 117(3), 572–582.

Murphy, A. H. (1988). "Skill scores based on the mean square error and their relationships to the correlation coefficient." *Mon. Weather Rev.*, 116(12), 2417–2424.

Navidi, W. (2006). *Statistics for engineers and scientists*, McGraw-Hill, New York.

Neary, V., and Sotiropoulos, F. (1996). "Numerical investigation of laminar flows through 90-degree diversions of rectangular cross-section." *Comput. Fluids*, 25(2), 95–118.

Nidzieko, N. J., Hench, J. L., and Monismith, S. G. (2009). "Lateral circulation in well-mixed and stratified estuarine flows with curvature." *J. Phys. Oceanogr.*, 39(4), 831–851.

Ralston, D. K., Geyer, W. R., and Lerczak, J. A. (2010). "Structure, variability, and salt flux in a strongly forced salt wedge estuary." *J. Geophys. Res. Oceans*, 115(C6).

Ramamurthy, A., Qu, J., and Vo, D. (2007). "Numerical and experimental study of dividing open-channel flows." *J. Hydraul. Eng.*, 10.1061/(ASCE)0733-9429(2007)133:10(1135), 1135–1144.

Signell, R. P., and Butman, B. (1992). "Modeling tidal exchange and dispersion in Boston Harbor." *J. Geophys. Res. Oceans*, 97(C10), 15591–15606.

Smith, R., and Daish, N. (1991). "Dispersion far downstream of a river junction." *Phys. Fluids A*, 3(5), 1102.

Wang, B., Fringer, O., Giddings, S., and Fong, D. (2009). "High-resolution simulations of a macrotidal estuary using SUNTANS." *Ocean Modell.*, 28(1–3), 167–192.

Wang, B., Giddings, S., Fringer, O., Gross, E., Fong, D., and Monismith, S. (2011). "Modeling and understanding turbulent mixing in a macrotidal salt wedge estuary." *J. Geophys. Res. Oceans*, 116(C2), in press.

Warner, J. C., Sherwood, C. R., Arango, H. G., and Signell, R. P. (2005). "Performance of four turbulence closure models implemented using a generic length scale method." *Ocean Modell.*, 8(1), 81–113.

Weber, L., Schumate, E., and Mawer, N. (2001). "Experiments on flow at a 90-degree open-channel junction." *J. Hydraul. Eng.*, 10.1061/(ASCE)0733-9429(2001)127:5(340), 340–350.

Wolfram, P., and Fringer, O. (2013). "Mitigating horizontal divergence "checker-board" oscillations on unstructured triangular C-grids for non-linear hydrostatic and nonhydrostatic flows." *Ocean Modell.*, 69, 64–78.

Wolfram, P. J. (2013). "Secondary flows and dispersion in channel junctions." Ph.D. thesis, Stanford Univ., Stanford, CA.